Giant Transport Anisotropy in math xmlns="http://www.w3.org/1998/Math/MathML" display="inline">mrow>msub>mrow>mi>ReS/mi>/mrow >mrow>mn>2/mn>/mrow>/msub>/mrow>/math> Revealed via Nanoscale Conducting-Path Control

Dawei Li, Shuo Sun, Zhiyong Xiao, Jingfeng Song, Ding-Fu Shao, Evgeny Y. Tsymbal, Stephen Ducharme, and Xia Hong

Phys. Rev. Lett. **127**, 136803 — Published 24 September 2021

DOI: 10.1103/PhysRevLett.127.136803

Giant Transport Anisotropy in ReS_2 Revealed via Nanoscale Conducting Path Control

Dawei Li,[1] Shuo Sun,[1] Zhiyong Xiao,[1] Jingfeng Song,[1] Ding-Fu Shao,[1] Evgeny Y. Tsymbal,[1] Stephen Ducharme,[1] Xia Hong[1*]

[1] Department of Physics and Astronomy & Nebraska Center for Materials and Nanoscience, University of Nebraska-Lincoln, Lincoln, Nebraska 68588-0299, USA

[*] Correspondence to: xia.hong@unl.edu

Abstract

The low in-plane symmetry in layered 1T'-ReS_2 results in strong band anisotropy, while its manifestation in the electronic properties is challenging to resolve due to the lack of effective approaches for controlling the local current path. In this work, we reveal the giant transport anisotropy in monolayer to four-layer ReS_2 by creating directional conducting paths via nanoscale ferroelectric control. By reversing the polarization of a ferroelectric polymer top layer, we induce conductivity switching ratio of $>1.5\times10^8$ in the ReS_2 channel at 300 K. Characterizing the domain-defined conducting nanowires in an insulating background shows that the conductivity ratio between the directions along and perpendicular to the Re-chain can exceed 5.5×10^4 in monolayer MoS_2. Theoretical modeling points to the band origin of the transport anomaly, and further reveals the emergence of a flat band in few-layer ReS_2. Our work paves the path for implementing the highly anisotropic 2D materials for designing novel collective phenomena and electron lensing applications.

Layered two-dimensional (2D) semiconductors such as black phosphorus and 1T'-rhenium disulfide (ReS_2) possess low in-plane symmetry, which leads to a rich spectrum of intriguing electronic and optical phenomena [1], including intrinsic band anisotropy [2], strongly anisotropic bound excitons and nonlinear optical responses [3-6], tunable hyperbolic plasmonics [7-9], large optical birefringence [10, 11], moiré superlattices [12-14], and multiferroic behaviors [15, 16]. The transition metal dichalcogenide (TMDC) ReS_2 is a direct band gap semiconductor, with the band gap (E_g) varying from 1.43 eV in monolayer samples to 1.35 eV in bulk [17]. It exhibits strong intra-layer anisotropy between the directions along and perpendicular to the Re chains. Theoretical studies have shown that the band dispersions lead to highly direction-dependent mobility in ReS_2 [18, 19], while direct mapping of its angle-resolved transport remains challenging due to the lack of effective strategies to control the local current path [20, 21].

A promising approach to define reconfigurable, directional conduction paths in the 2D semiconductors is to leverage the nanoscale controllable polarization of an adjacent ferroelectric layer. In previous studies, ferroelectric domain patterning has been exploited to impose a wide range of functionalities in TMDCs [22, 23], including programmable homo- and hetero-junction states [24, 25] and photovoltaic effects [26], nanoscale excitonic modulation [27, 28], and nonlinear optical filtering [29]. Combining local polarization writing with the ferroelectric field effect enables the programming of nanoscale conduction paths within an insulating background, which can confine the local current flow in pre-designed directions on the same sample. Unlike lithographically defined nanowires, the nonvolatile field effect approach is clean, reversible, and does not involve uncontrollable sample-to-sample variations.

In this work, we exploited nanoscale polarization control of a ferroelectric copolymer poly(vinylidene fluoride-trifluoroethylene) [P(VDF-TrFE)] top layer to probe the transport

anisotropy in atomically thin ReS_2. By characterizing the domain-defined conducting nanowires in the insulating channel [Fig. 1(a)], we mapped out the angle-resolved conductance of single-layer (1L), bilayer (2L), and four-layer (4L) ReS_2 field effect transistors (FETs), which revealed a giant conductivity ratio of 5.5×10^4 between the directions along and perpendicular to the Re-chain [Fig. 1(b)]. The transport results can be well accounted for by the band anisotropy in conjunction with the electron-phonon scattering, as revealed by our first-principles density functional theory (DFT) modeling, which further points to the emergence of a flat band in the 4L ReS_2. Our study illustrates a powerful approach for resolving nanoscale electronic signatures of emergent band properties in van der Waals (vdW) materials, as well as presenting a promising material platform for realizing topology and correlation-driven quantum phenomena.

We mechanically exfoliated monolayer and few-layer ReS_2 flakes from bulk single crystals onto the Gel-Films. The layer number was confirmed by atomic force microscopy (AFM, Bruker MultiMode 8) studies combined with the Raman frequency difference Δ between the modes I and III. The crystalline orientation of ReS_2 was identified by angle-resolved parallel-polarized Raman scattering measurements (Supplemental Materials) [30, 31]. Selected 1-4L ReS_2 flakes were transferred onto SiO_2 (290 nm)/doped Si substrates pre-patterned with Cr/Au (2 nm/10 nm) electrodes, forming FET devices. Next, we deposited 9 monolayers of P(VDF-TrFE) film on top of ReS_2 using the Langmuir-Blodgett (LB) technique [32] followed by a thermal annealing treatment at 135 ^oC for 80 min (Supplemental Materials) [30]. Our previous studies have shown that the thermally treated P(VDF-TrFE) on ReS_2 is single crystalline with the polar axis along the film normal [33]. To switch the ferroelectric polarization, a ±11 V DC bias (V_{bias}) was applied to a conductive PtIr-coated tip (Bruker SCM-PIC-V2), with domain writing controlled by the NanoMan program. The resulting domain structures were imaged using piezoresponse force

microscopy (PFM). The electrical characterization was performed using the semiconductor parameter analyzer (Keysight B1500A) after domain patterning, while the sample was kept in the AFM during the entire process.

Figures 1(c)-(e) display the PFM phase images taken on a 1L ReS_2 FET, with the P(VDF-TrFE) top layer in the as-prepared, no poling state [Fig. 1(c)] and the uniformly patterned polarization down (P_{down}) [Fig. 1(d)] and up (P_{up}) [Fig. 1(e)] states, respectively. In all states, the sample exhibits linear source-drain current-voltage (I_d-V_d) relation, confirming the Ohmic characteristic (Supplemental Fig. S3) [30]. Figure 1(f) compares the I_d versus back-gate voltage (V_{bg}) relation for these three states, showing the P_{down} (P_{up}) state accumulates (depletes) electrons in ReS_2, as expected. The transfer curve in the P_{up} state exhibits hole-doped characteristic, with I_d decreasing with increasing V_{bg}. In contrast, the P_{down} polarization of P(VDF-TrFE) introduces a high level of electron-doping in ReS_2, changing the dominant carrier type from *p*-type to *n*-type. In this state, the ReS_2 channel remains highly conductive over the entire V_{bg}–range, showing that the accumulated electron density well exceeds what can be effectively depleted by the SiO_2 back-gate. The current switching ratio between the P_{down} and P_{up} states reaches 5.3×10^6 at V_{bg} = 7 V. A higher switching ratio may be expected at $+7\ V \leq V_{bg} \leq +40$ V, where the 1L ReS_2 becomes so insulating in the P_{up} state that the current level is below the instrument resolution.

We also achieved nonvolatile current modulation in the 2L and 4L ReS_2 FET devices [Fig. 1(g) and Supplemental Fig. S3] [30]. In the 4L device, we extracted from the transfer curves a high current switching ratio of 1.5×10^8 at V_{bg} = 12 V, which is among the highest values reported in ferroelectric-gated 2D FETs [34]. Compared with the polymorphous polymer films prepared via spin coating [21], where the net polarization is compromised due to the randomly oriented polar grains, the thermally treated LB films enable the remarkable level of doping modulation, which is

critical for defining a highly insulating background. In the P_{up} state, both channels exhibit a transition from *p*-type to *n*-type transfer characteristics with increasing V_{bg}, indicating that the Fermi level is shifted close to the conduction band. Even though the fractional change of the doping level is expected to increase with decreasing channel thickness, we find the ferroelectric field effect is larger in the thicker samples. A likely reason is 1L MoS_2 is highly insulating in the P_{up} state and cannot provide sufficient screening to P(VDF-TrFE). This results in a high depolarization field, which leads to incomplete polarization switching [23].

To create a directional conducting nanowire, we switched the polarization of P(VDF-TrFE) into the uniform P_{up} state, setting the entire ReS_2 channel in a highly insulating state, and then wrote a line-shaped P_{down} domain between the source and drain. Given the high current switching ratio, the nanowire conductance remains orders of magnitude higher than the insulating background over the entire V_{bg}-range. We worked with P_{down} nanowires that are 300-400 nm wide. At this width range, electron conduction can be effectively confined to be along the nanowire direction, while the nanowire can sustain the 2D transport characteristic without a prominent edge contribution. Writing P_{down} nanowire domains along different orientations thus enables angle-resolved conductance measurements on the same sample. Figure 2 shows the results obtained on a 1L ReS_2 FET using this approach. The *b*-axis of this sample is perpendicular to the channel orientation [Fig. 2(a)] [30]. We wrote a series of P_{down} nanowires connecting the source and drain electrodes [Figs. 2(b)-2(e)]. Figure 2(f) shows the corresponding channel sheet conductance $\sigma = \frac{L}{W}\frac{I_d}{V_d}$, or 2D conductivity, as a function of V_{bg} for the nanowires. Here L and W are the length and width of the nanowire, respectively, and the angle θ is defined with respect to the *b*-axis of ReS_2. It is evident that there are two distinct transfer characteristics for these four angles. For the nanowire along the directions of $\theta = 30^o$ and 150^o, which are oriented close to the *b*-axis, the

channel remains highly conductive with *n*-type characteristic over the entire V_{bg}-range. In contrast, for $\theta = 75^{o}$ and 90^{o}, which are close to the direction perpendicular to the *b*-axis, the ReS_2 nanowires exhibit very low conductance, with the channel effectively turned into *p*-type at $V_{bg} < 20\,V$. At $V_{bg} = 20$ V, ReS_2 exhibits up to 5.5×10^{4}-fold change in conductance between the directions of $\theta = 30^{o}$ and $\theta = 75^{o}$, which also corresponds to a change of carrier type from electron- to hole-doped behavior. An even larger transport anisotropy is expected between $V_{bg} =$ 20 V and 35 V, where the channel is too insulating along $\theta = 75^{o}$ direction to be measured.

To map out the angle-resolved transport close to the conduction band edge, we extracted the conductivity of nanowires in various directions at fixed V_{bg}. We chose a V_{bg} at which the sample is at the threshold of turned on and electron-doped in all directions. Figures 3(a) shows the polar plot of σ for the 1L ReS_2 sample at V_{bg} = 40 V. The sheet conductance measured at the angles $\theta = 30^{o}$ (954 nS)) is about 56 times of that at $\theta = 105^{o}$ (17 nS). Similar electron conduction anisotropy has been observed in the 2L [Fig. 3(b)] and 4L [Fig. 3(c)] ReS_2 samples (Supplemental Materials) [30]. Despite the fluctuation of the data points, which can be affected by the local defects in the P(VDF-TrFE) top-layer close to the nanowire area, all samples exhibit high conductance in the vicinity of the *b*-axis ($\theta = 0^{o}$) and low conductance when θ approaches 90^{o}. The anisotropy is strongly enhanced in the few-layer sample, with a giant anisotropic conductance ratio of 1.7×10^{3} observed in the 4L ReS_2 device between the directions of $\theta = 0^{o}$ (496.5 nS) and 120^{o} (0.3 nS) [Fig. 3(c)]. Unlike the modulation observed in Fig. 2(f), this change does not involve the change of carrier type, thus reflecting solely the electron transport anisotropy. Note that the observed angular dependence of σ reflects a lack of mirror symmetry with respect to the $\theta = 0°$ axis. As 1T'-ReS_2 belongs to the space group $P\bar{1}$, it only has an inversion symmetry.

The conductance in ReS_2 is determined by the electron mobility $\mu = e\tau/m^*$, where e is the electron charge, τ is the average scattering time induced by defects, impurities, or phonons, and m^* is the effective mass determined by the band structure $E(\boldsymbol{k})$ as $m^* = \frac{\hbar^2}{\partial^2 E(\boldsymbol{k})/\partial \boldsymbol{k}^2}$. To understand the role of band dispersion on the anisotropic conduction, we performed the first-principles DFT calculations for the band structures of 1L [Fig. 4(a)], 2L [Fig. 4(b)], and 4L [Fig. 4(c)] ReS_2. The details of the calculation can be found in the Supplemental Materials [30, 35-38]. The result obtained for 1L ReS_2 is consistent with the previous report [20]. For all three layer numbers, the band dispersion along the k_x direction (b-axis) at the conduction band minimum (CBM) exhibits a larger curvature compared with that along the k_y direction [Figs. 4(d)-(f)], yielding a lighter m^* along b-axis ($\theta = 0°$) and a heavier m^* perpendicular to b-axis ($\theta = 90°$). The anisotropy of the band dispersion, on the other hand, is significantly enhanced with increasing layer thickness of ReS_2. For all layer thicknesses, the inversion symmetry of the space group $P\bar{1}$ has been preserved in the calculated m^* (Supplemental Materials) [30].

Figures 4(g)-(i) show the normalized $1/m^*$ *vs.* θ relation superimposed onto the normalized conductance (σ_{norm}) data. For 1L ReS_2, $1/m^*$ shows a similar θ −dependence as the measured σ, *i.e.*, the maximum values appear at orientations close to $\theta = 0°$ and 180° and the minimum values appear close to $\theta = 90°$ and 270° directions [Fig. 4(g)]. The variation in $1/m^*$, however, cannot fully account for the relative change in σ_{norm}. Considering that the band anisotropy also affects the election-phonon scattering, we incorporated the contribution of phonon scattering in mobility μ by using the Takagi formula [39-41]:

$$\mu_i = \frac{e\hbar^3 C_i}{k_B T m_i^* m_d^* D_i^2}\,. \qquad (1)$$

Here i refers to the conduction direction, and $m_d^* = \sqrt{m_x^* m_y^*}$ is the density-of-state effective mass for an anisotropic electronic band. The deformation potential constant is defined as $D_i = \frac{\partial E_V}{\partial \varepsilon_i}$, where E_V is the energy of the CBM and ε_i is a strain applied along direction i. The 2D elastic modulus along the conduction direction is calculated using $C_i = \frac{2\partial^2 E_{\text{total}}}{S_0 \partial {\varepsilon_i}^2}$, where E_{total} is the total energy of ReS_2 and S_0 is the area of the 2D ReS_2 without strain. As shown in Fig. 4(g), the modeled μ *vs.* θ relation shows improved agreement with $\sigma_{\text{norm}}(\theta)$, indicating that the anisotropic conductance in 1L ReS_2 is resulted from the convoluted effects of the anisotropic band dispersion and the phonon scattering. On the other hand, we find that $\sigma_{\text{norm}}(\theta)$ for the 2L [Fig. 4(h)] and 4L [Fig. 4(i)] ReS_2 can be well explained by the calculated $1/m^*$ *vs.* θ relation. This is because the anisotropy of the conduction band dispersion is significantly enhanced in thicker ReS_2 [Figs. 4(d)-(f)], so that the angular dependence of electron-phonon scattering plays a relatively minor role in the electron transport in 2L and 4L ReS_2.

These findings are in sharp contrast with the previous study of angle-resolved transport in ReS_2 using a circular sample geometry with multiple point-contacts along various directions [20] or micron-sized conduction channels [21], where the experimentally extracted anisotropic conductance ratio is significantly smaller than the theoretical prediction. In both approaches, the local current path within the sample cannot be well controlled. The measurements thus collect current flows over a wide range of angle distributions, making it challenging to quantitatively analyze the directional conduction.

What is intriguing is the emergence of a nearly flat band in 4L ReS_2 at the CBM along the k_y direction [Fig. 4 (f)], leading to a drastic increase in m^* for $\theta = 90°$ (Supplemental Materials), which can well account for the giant electron transport anisotropy observed in 4L ReS_2 [30]. Such band dispersion highly resembles what is predicted for one-dimensional graphene superlattices

(GSL) [42]. It is thus conceivable to design ReS_2-based novel electron lensing applications by either varying the layer numbers along the conducting path through assembling artificial ReS_2 heterostructures or integrating few-layer ReS_2 with other isotropic vdW materials. Compared with the GSL approach, which is challenging to realize due to difficulties in imposing nanoscale 1D periodic potential, few-layer ReS_2-based electron supercollimation builds upon the fabrication of vdW heterostructure and is free of lithography induced disorder and fluctuation. The flat band and the associated heavy effective mass also make few-layer ReS_2 a promising platform for hosting collective phenomena, such as magnetism and superconductivity.

In summary, we have resolved for the first time the giant transport anisotropy in mono- to few-layer ReS_2 by creating directional conducing paths through the nanoscale ferroelectric control, which reveals a 2D conductivity ratio exceeding 5.5×10^4 between the directions along and perpendicular to *b*-axis in 1L ReS_2. Our DFT calculations point to the band origin of this intriguing behavior, and revealed the emergence of a flat band in few-layer ReS_2. Our approach can be widely applicable to other anisotropic vdW materials, providing a novel route for resolving nanoscale electronic signatures of emergent band properties and designing collective phenomena and electron lensing applications in vdW heterostructures.

Acknowledgements

We thank Xi Huang and Yongfeng Lu for the access to the Raman system. This work was primarily supported by the U.S. Department of Energy (DOE), Office of Science, Basic Energy Sciences (BES), under Award No. DE-SC0016153 (sample preparation and characterization, FET device fabrication and characterization). S.S. and S.D. acknowledge the support of the Nebraska Center for Energy Research. The work of D.-F.S. and E.Y.T. was supported by the NSF Nebraska

Materials Research Science and Engineering Center (MRSEC) Grant No. DMR-1420645 (theoretical modeling). The research was performed in part in the Nebraska Nanoscale Facility: National Nanotechnology Coordinated Infrastructure and the Nebraska Center for Materials and Nanoscience, which are supported by the National Science Foundation under Award ECCS: 2025298, and the Nebraska Research Initiative.

References

[1] S. Barraza-Lopez, F. Xia, W. Zhu, and H. Wang, Beyond Graphene: Low-Symmetry and Anisotropic 2D Materials, Journal of Applied Physics **128**, 140401 (2020).

[2] C. Gong, Y. Zhang, W. Chen, J. Chu, T. Lei, J. Pu, L. Dai, C. Wu, Y. Cheng, T. Zhai, L. Li, and J. Xiong, Electronic and Optoelectronic Applications Based on 2D Novel Anisotropic Transition Metal Dichalcogenides, Advanced Science **4**, 1700231 (2017).

[3] X. Wang, A. M. Jones, K. L. Seyler, V. Tran, Y. Jia, H. Zhao, H. Wang, L. Yang, X. Xu, and F. Xia, Highly anisotropic and robust excitons in monolayer black phosphorus, Nature Nanotechnology **10**, 517 (2015).

[4] X. Meng, Y. Zhou, K. Chen, R. H. Roberts, W. Wu, J. F. Lin, R. T. Chen, X. Xu, and Y. Wang, Anisotropic Saturable and Excited- State Absorption in Bulk ReS_2, Advanced Optical Materials **6**, 1800137 (2018).

[5] Q. Cui, R. A. Muniz, J. Sipe, and H. Zhao, Strong and anisotropic third-harmonic generation in monolayer and multilayer ReS_2, Physical Review B **95**, 165406 (2017).

[6] D. Li, C. Wei, J. Song, X. Huang, F. Wang, K. Liu, W. Xiong, X. Hong, B. Cui, and A. Feng, Anisotropic enhancement of second-harmonic generation in monolayer and bilayer MoS_2 by integrating with TiO_2 nanowires, Nano Letters **19**, 4195 (2019).

[7] A. Nemilentsau, T. Low, and G. Hanson, Anisotropic 2D materials for tunable hyperbolic plasmonics, Physical Review Letters **116**, 066804 (2016).

[8] C. Wang, G. Zhang, S. Huang, Y. Xie, and H. Yan, The Optical Properties and Plasmonics of Anisotropic 2D Materials, Advanced Optical Materials **8**, 1900996 (2020).

[9] T. Low, A. Chaves, J. D. Caldwell, A. Kumar, N. X. Fang, P. Avouris, T. F. Heinz, F. Guinea, L. Martin-Moreno, and F. Koppens, Polaritons in layered two-dimensional materials, Nature Materials **16**, 182 (2017).

[10] H. Yang, H. Jussila, A. Autere, H.-P. Komsa, G. Ye, X. Chen, T. Hasan, and Z. Sun, Optical Waveplates Based on Birefringence of Anisotropic Two-Dimensional Layered Materials, ACS Photonics **4**, 3023 (2017).

[11] N. Papadopoulos, R. Frisenda, R. Biele, E. Flores, J. R. Ares, C. Sánchez, H. S. J. van der Zant, I. J. Ferrer, R. D'Agosta, and A. Castellanos-Gomez, Large birefringence and linear dichroism in TiS_3 nanosheets, Nanoscale **10**, 12424 (2018).

[12] Z. Qiu, M. Trushin, H. Fang, I. Verzhbitskiy, S. Gao, E. Laksono, M. Yang, P. Lyu, J. Li, J. Su, M. Telychko, K. Watanabe, T. Taniguchi, J. Wu, A. H. C. Neto, L. Yang, G. Eda, S. Adam, and J. Lu, Giant gate-tunable bandgap renormalization and excitonic effects in a 2D semiconductor, Science Advances **5**, eaaw2347 (2019).

[13] Y. Liu, J. N. B. Rodrigues, Y. Z. Luo, L. Li, A. Carvalho, M. Yang, E. Laksono, J. Lu, Y. Bao, H. Xu, S. J. R. Tan, Z. Qiu, C. H. Sow, Y. P. Feng, A. H. C. Neto, S. Adam, J. Lu, and K. P. Loh, Tailoring sample-wide pseudo-magnetic fields on a graphene–black phosphorus heterostructure, Nature Nanotechnology **13**, 828 (2018).

[14] R. Plumadore, M. M. Al Ezzi, S. Adam, and A. Luican-Mayer, Moiré patterns in graphene–rhenium disulfide vertical heterostructures, Journal of Applied Physics **128**, 044303 (2020).

[15] S. Barraza-Lopez, B. M. Fregoso, J. W. Villanova, S. S. Parkin, and K. Chang, Colloquium: Physical properties of group-IV monochalcogenide monolayers, arXiv:2009.04341 (2020).

[16] F. Xia, H. Wang, J. C. M. Hwang, A. H. C. Neto, and L. Yang, Black phosphorus and its isoelectronic materials, Nature Reviews Physics **1**, 306 (2019).

[17] S. Tongay, H. Sahin, C. Ko, A. Luce, W. Fan, K. Liu, J. Zhou, Y.-S. Huang, C.-H. Ho, J. Yan, D. F. Ogletree, S. Aloni, J. Ji, S. Li, J. Li, F. M. Peeters, and J. Wu, Monolayer behaviour in bulk ReS2 due to electronic and vibrational decoupling, Nature Communications **5**, 3252 (2014).

[18] J. L. Webb, L. S. Hart, D. Wolverson, C. Chen, J. Avila, and M. C. Asensio, Electronic band structure of ReS_2 by high-resolution angle-resolved photoemission spectroscopy, Physical Review B **96**, 115205 (2017).

[19] B. S. Kim, W. Kyung, J. Denlinger, C. Kim, and S. Park, Strong One-Dimensional Characteristics of Hole-Carriers in ReS 2 and ReSe 2, Scientific reports **9**, 1 (2019).

[20] E. Liu, Y. Fu, Y. Wang, Y. Feng, H. Liu, X. Wan, W. Zhou, B. Wang, L. Shao, and C.-H. Ho, Integrated digital inverters based on two-dimensional anisotropic ReS_2 field-effect transistors, Nature communications **6**, 1 (2015).

[21] R. Wang, F. Zhou, L. Lv, S. Zhou, Y. Yu, F. Zhuge, H. Li, L. Gan, and T. Zhai, Modulation of the Anisotropic Electronic Properties in ReS_2 via Ferroelectric Film, CCS Chemistry **1**, 268 (2019).

[22] X. Hong, Emerging ferroelectric transistors with nanoscale channel materials: the possibilities, the limitations, Journal of Physics: Condensed Matter **28**, 103003 (2016).

[23] H. Ryu, K. Xu, D. Li, X. Hong, and W. Zhu, Empowering 2D nanoelectronics via ferroelectricity, Applied Physics Letters **117**, 080503 (2020).

[24] Z. Xiao, J. Song, D. K. Ferry, S. Ducharme, and X. Hong, Ferroelectric-Domain-Patterning-Controlled Schottky Junction State in Monolayer MoS_2, Physical Review Letters **118**, 236801 (2017).

[25] G. Wu, B. Tian, L. Liu, W. Lv, S. Wu, X. Wang, Y. Chen, J. Li, Z. Wang, S. Wu, H. Shen, T. Lin, P. Zhou, Q. Liu, C. Duan, S. Zhang, X. Meng, S. Wu, W. Hu, X. Wang, J. Chu, and J. Wang, Programmable transition metal dichalcogenide homojunctions controlled by nonvolatile ferroelectric domains, Nature Electronics **3**, 43 (2020).

[26] L. Lv, F. Zhuge, F. Xie, X. Xiong, Q. Zhang, N. Zhang, Y. Huang, and T. Zhai, Reconfigurable two-dimensional optoelectronic devices enabled by local ferroelectric polarization, Nature Communications **10**, 1 (2019).

[27] C. H. Li, K. M. McCreary, and B. T. Jonker, Spatial Control of Photoluminescence at Room Temperature by Ferroelectric Domains in Monolayer WS_2/PZT Hybrid Structures, ACS Omega **1**, 1075 (2016).

[28] B. Wen, Y. Zhu, D. Yudistira, A. Boes, L. Zhang, T. Yidirim, B. Liu, H. Yan, X. Sun, and Y. Zhou, Ferroelectric-driven exciton and trion modulation in monolayer molybdenum and tungsten diselenides, ACS Nano **13**, 5335 (2019).

[29] D. Li, X. Huang, Z. Xiao, H. Chen, L. Zhang, Y. Hao, J. Song, D.-F. Shao, E. Y. Tsymbal, Y. Lu, and X. Hong, Polar coupling enabled nonlinear optical filtering at MoS_2/ferroelectric heterointerfaces, Nature Communications **11**, 1422 (2020).

[30] See Supplemental Material at URL for the details of sample characterization, electrical measurments, and theoretical calculations.

[31] D. A. Chenet, O. B. Aslan, P. Y. Huang, C. Fan, A. M. van der Zande, T. F. Heinz, and J. C. Hone, In-Plane Anisotropy in Mono- and Few-Layer ReS2 Probed by Raman Spectroscopy and Scanning Transmission Electron Microscopy, Nano Letters **15**, 5667 (2015).

[32] S. Ducharme, S. P. Palto, V. M. Freidkin, and L. M. Blinov, *Ferroelectric Polymer Langmuir-Blodgett Films* (Academic Press, San Diego, 2002), Vol. 3.

[33] D. Li, S. Sun, K. Wang, Z. Ahmadi, J. E. Shield, Stephen Ducharme, and X. Hong, Assembly of Close-Packed Ferroelectric Polymer Nanowires via Interface-Epitaxy with ReS_2, Advanced materials, *Accepted* (2021).

[34] S. Bertolazzi, P. Bondavalli, S. Roche, T. San, S. Y. Choi, L. Colombo, F. Bonaccorso, and P. Samorì, Nonvolatile memories based on graphene and related 2D materials, Advanced Materials **31**, 1806663 (2019).

[35] P. E. Blöchl, Projector augmented-wave method, Physical review B **50**, 17953 (1994).

[36] G. Kresse, and D. Joubert, From ultrasoft pseudopotentials to the projector augmented-wave method, Physical Review B **59**, 1758 (1999).

[37] J. P. Perdew, K. Burke, and M. Ernzerhof, Generalized gradient approximation made simple, Physical Review Letters **77**, 3865 (1996).

[38] S. Grimme, J. Antony, S. Ehrlich, and H. Krieg, A consistent and accurate ab initio parametrization of density functional dispersion correction (DFT-D) for the 94 elements H-Pu, Journal of Chemical Physics **132**, 154104 (2010).

[39] S.-i. Takagi, A. Toriumi, M. Iwase, and H. Tango, On the universality of inversion layer mobility in Si MOSFET's: Part I-effects of substrate impurity concentration, IEEE Transactions on Electron Devices **41**, 2357 (1994).

[40] S.-i. Takagi, A. Toriumi, M. Iwase, and H. Tango, On the universality of inversion layer mobility in Si MOSFET's: Part II-effects of surface orientation, IEEE Transactions on Electron Devices **41**, 2363 (1994).

[41] S. Poncé, W. Li, S. Reichardt, and F. Giustino, First-principles calculations of charge carrier mobility and conductivity in bulk semiconductors and two-dimensional materials, Reports on Progress in Physics **83**, 036501 (2020).

[42] C.-H. Park, Y.-W. Son, L. Yang, M. L. Cohen, and S. G. Louie, Electron Beam Supercollimation in Graphene Superlattices, Nano Letters **8**, 2920 (2008).

Captions:

FIG. 1. (a) Device schematic. (b) Schematic crystal structure of ReS_2. (c-e) PFM phase images of a 1L ReS_2 FET (1L-D1) with the P(VDF-TrFE) top-gate (c) in the initial no-poling state, and uniformly polarized in the (d) P_{down} and (e) P_{up} (bottom) states. (f) I_d *vs.* V_{bg} for the 1L ReS_2 FET in (c-e) in the P_{down}, P_{up}, and no poling states of P(VDF-TrFE). (g) I_d *vs.* V_{bg} for a 4L ReS_2 in different polar states of P(VDF-TrFE).

FIG. 2. (a) Optical image of a 1L ReS_2 device. Insets: laboratory coordinates (left) and crystalline axes of ReS_2 (right). (b-e) PFM phase images of P_{down} nanowires created on the uniform P_{up} background along (b) $\theta = 30^o$, (c) $\theta = 75^o$, (d) $\theta = 90^o$, and (e) $\theta = 150^o$ directions with respect to *b*-axis of ReS_2. (f) The corresponding σ *vs.* V_{bg}.

FIG. 3. Polar plots of σ of (a) a 1L ReS_2 at V_{bg} = 40 V, (b) a 2L ReS_2 at V_{bg} = -40 V, and (c) a 4L ReS_2 at V_{bg} = 10 V. The dashed lines serve as the guide to the eye. Insets in (b): PFM images of the corresponding P_{down} nanowires. The top left image corresponds to the initial uniform P_{up} domain before the nanowire patterning. All scale bars are 3 μm.

FIG. 4. (a-c) Band structures of (a) 1L, (b) 2L, and (c) 4L ReS_2. Insets in (a) show the symmetry points in the first Brillouin zone (left), where k_x and k_y are the same as *x*- and *y*-directions in the real space unit cell (right), with (d-f) the corresponding expanded views near the Γ point. (g) σ_{norm} *vs.* θ (left axis) for the 1L ReS_2 in Fig. 3a superimposed with the normalized $1/m^*_{norm}$ and m_{norm} (right axis). (h and i) σ_{norm} *vs.* θ (left axis) for (h) 2L and (i) 4L ReS_2 superimposed with $1/m^*_{norm}$ (right axis).

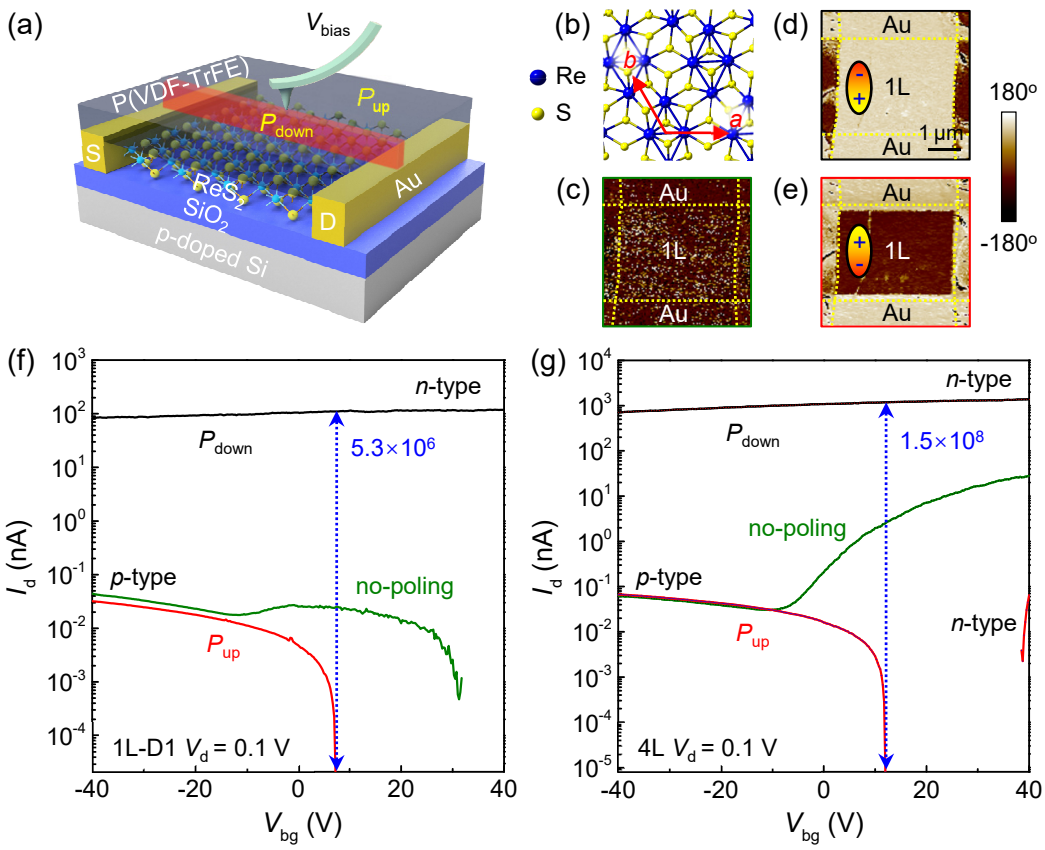
(a)
V_{bias}
P(VDF-TrFE)
P_{up}
P_{down}
S
D
Au
ReS_2
SiO_2
p-doped Si
(b)
Re
S
b
a
(c)
Au
1L
Au
(d)
Au
1L
Au
1 μm
(e)
Au
1L
Au
180°
-180°
(f)
n-type
P_{down}
5.3×10^6
p-type
no-poling
P_{up}
1L-D1 V_d = 0.1 V
I_d (nA)
V_{bg} (V)
(g)
n-type
P_{down}
1.5×10^8
no-poling
p-type
P_{up}
n-type
4L V_d = 0.1 V
I_d (nA)
V_{bg} (V)

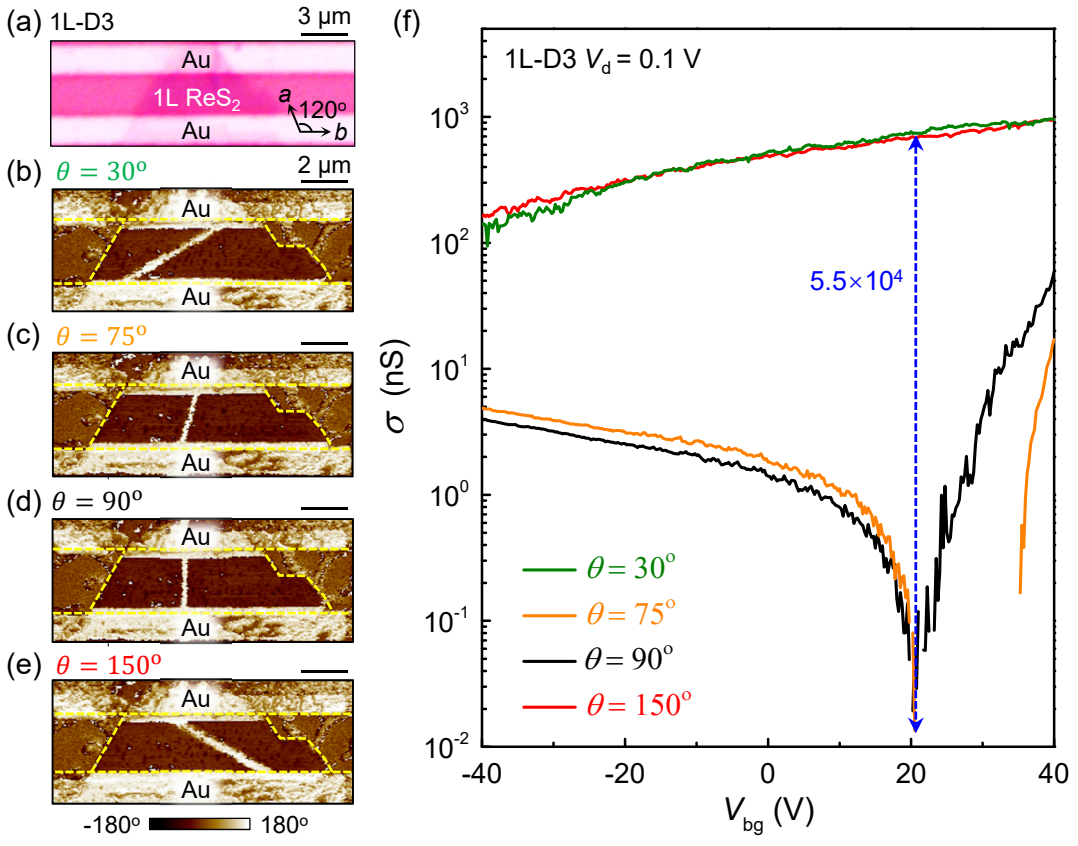
(a) 1L-D3
3 μm
Au
1L ReS2
a
120°
b
Au
(b) θ = 30°
2 μm
Au
Au
(c) θ = 75°
Au
Au
(d) θ = 90°
Au
Au
(e) θ = 150°
Au
Au
-180°
180°
(f)
1L-D3 Vd = 0.1 V
5.5×10⁴
σ (nS)
Vbg (V)
θ = 30°
θ = 75°
θ = 90°
θ = 150°

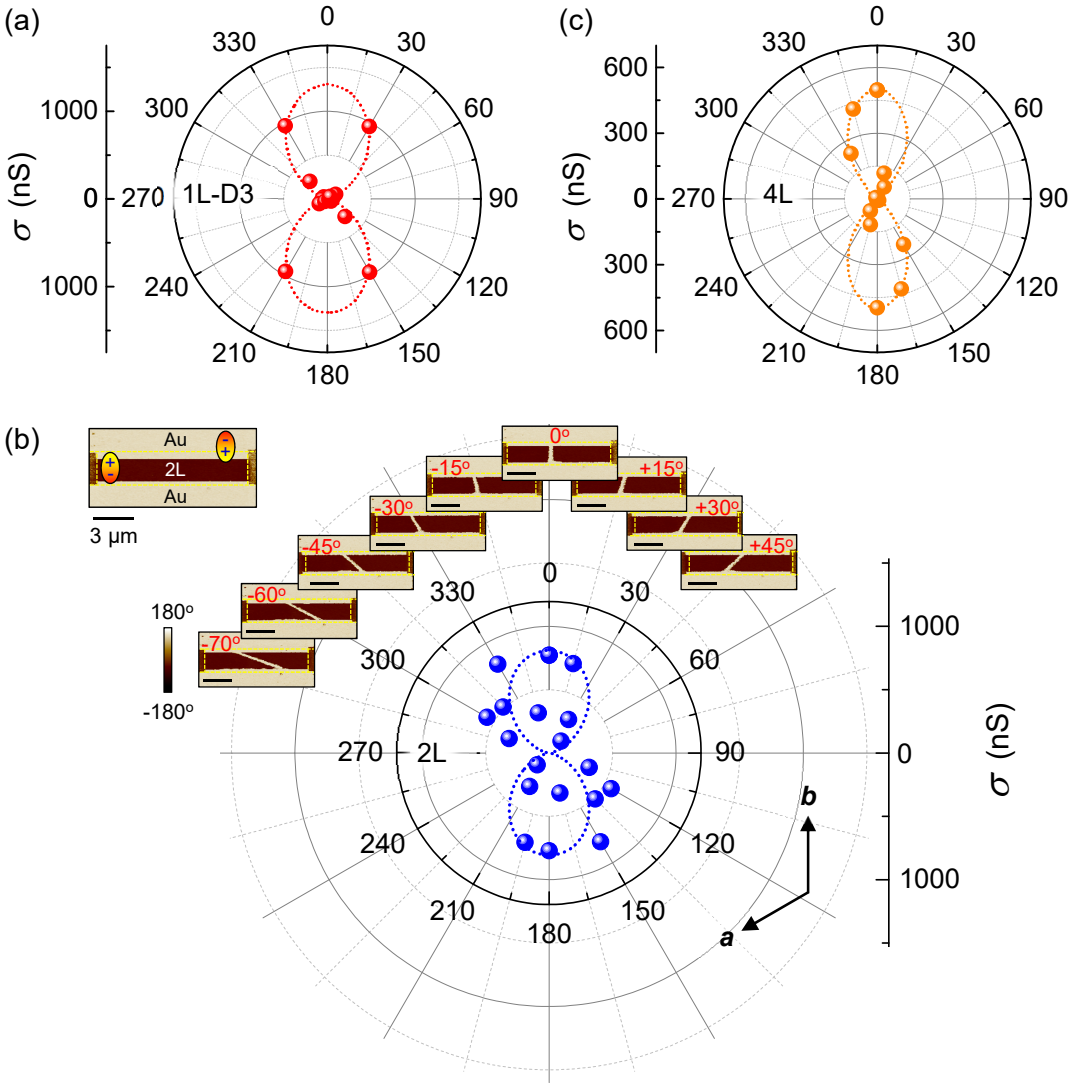
(a)
1L-D3
σ (nS)
1000
0
1000
0
30
60
90
120
150
180
210
240
270
300
330
(c)
4L
σ (nS)
600
300
0
300
600
(b)
Au
2L
Au
3 μm
180°
-180°
0°
-15°
+15°
-30°
+30°
-45°
+45°
-60°
-70°
2L
σ (nS)
1000
0
1000
b
a

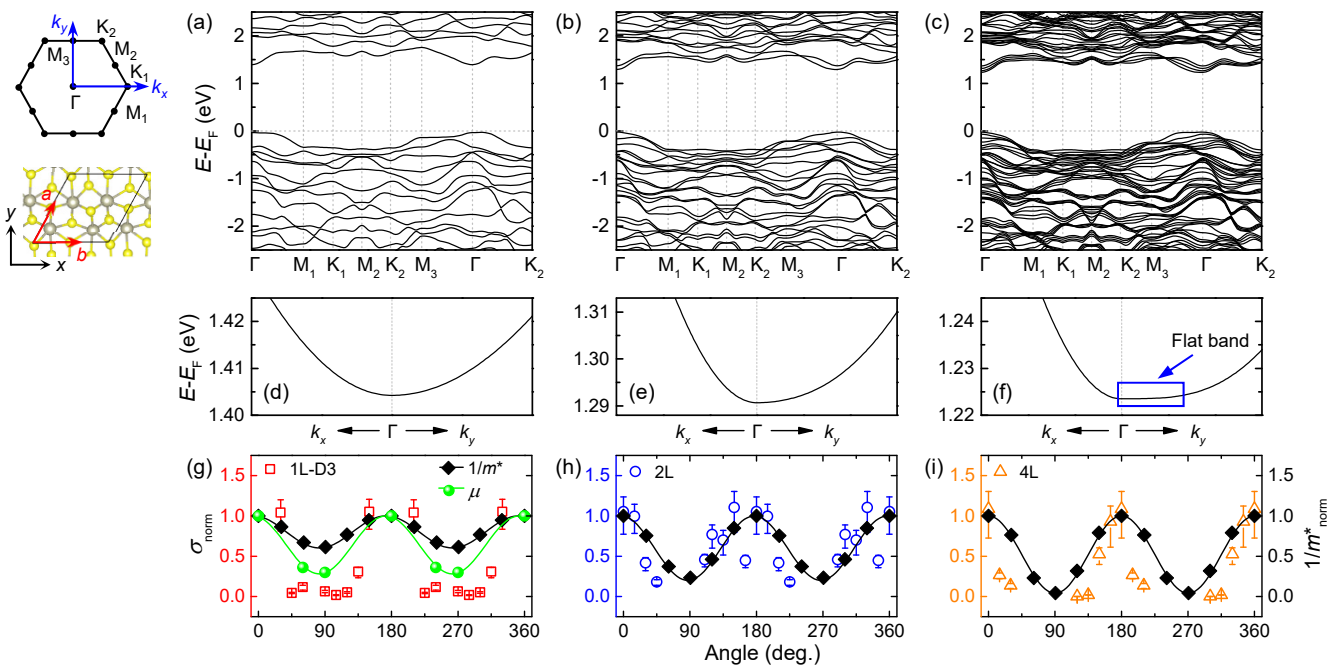
k_y
K_2
M_2
K_1
k_x
M_3
Γ
M_1
a
b
y
x
(a)
(b)
(c)
E-E_F (eV)
Γ M_1 K_1 M_2 K_2 M_3 Γ K_2
(d)
(e)
(f)
Flat band
k_x Γ k_y
(g)
1L-D3
$1/m^*$
μ
σ_{norm}
(h)
2L
(i)
4L
$1/m^*_{norm}$
Angle (deg.)